Iron valence in skutterudites: Transport and magnetic properties of $Co_{1-x}Fe_xSb_3$

J. Yang,[1] G. P. Meisner,[1] D. T. Morelli,[2] and C. Uher[3]
[1]*Materials and Processes Laboratory, GM R&D Center, Warren, Michigan 48090*
[2]*Delphi Automotive Systems Research Labs., Warren, Michigan 48090*
[3]*Department of Physics, University of Michigan, Ann Arbor, Michigan 48109*
(Received 7 December 1999; revised manuscript received 31 July 2000; published 11 December 2000)

Iron in the binary skutterudite compound $CoSb_3$ has a dramatic effect on transport and magnetic properties comparable to that of ''rattling'' guest atoms in filled skutterudite compounds. We have measured thermal conductivity, thermopower, electrical resistivity, Hall effect, x-ray diffraction, and magnetic susceptibility on a series of iron-doped compounds $Co_{1-x}Fe_xSb_3$ with $x=0$, 0.005, 0.01, 0.02, 0.05, and 0.10 prepared by induction melting and annealing. Our results show that the thermal conductivity is greatly reduced with iron doping. We observe that iron doping causes only a small rate of change in carrier concentration, ~0.03 holes/Fe atom for samples with $x \geqslant 1$ at. %, even though iron has one fewer electron in its outer shell (eight) than cobalt (nine). The room temperature thermopower is reduced with increasing iron content, and we observe phonon drag effects at low temperature. Our magnetization measurements show the development of a paramagnetic moment approaching 1.73 μ_B/Fe atom, consistent with trivalent iron in a low-spin d^5 electron configuration. The subtle role of iron in creating lattice defects in $CoSb_3$ that are responsible for the dramatic thermal conductivity reduction will also be discussed.

DOI: 10.1103/PhysRevB.63.014410 PACS number(s): 75.50.Bb, 66.70.+f, 72.15.Jf

I. INTRODUCTION

Recent developments in new thermoelectric materials have generated much interest in skutterudite compounds.[1] Binary skutterudite compounds are of the form MX_3, where the metal atom M can be Co, Ir, or Rh, and the nonmetal atom X can be P, As, or Sb.[2–4] One of the most interesting features of the binary skutterudites is that small guest atoms may be inserted into the large voids in the crystal structure and then ''rattle'' inside their oversized cages. Slack and Tsoukala[5] suggested that this rattling motion would cause strong scattering of the heat-carrying lattice waves (phonons), resulting in a dramatically reduced thermal conductivity compared to that of the binary (unfilled) parent compounds. This was first experimentally verified by Morelli and Meisner in Ce-filled skutterudites,[6] and subsequently by Sales *et al.* in La and Tl-filled skutterudites,[7,8] and by Nolas *et al.* in Yb-filled skutterudites.[9] Morelli *et al.* observed that not only Ce filling but also alloying with Fe on the Co site diminishes the thermal conductivity,[10] and a similar effect was also observed by Nolas, Cohn, and Slack,[11] Stokes, Ehrlich, and Nolas,[12] Anno *et al.*,[13] and Sales, Chakoumakos, and Mandrus.[8] Meisner *et al.*,[14] however, found that the thermal conductivity is not minimized for 100% filling of the voids, but rather for fractional filling near 50%. This effect was explained by considering such fractionally filled skutterudites as solid solutions of fully filled and unfilled end-member compounds. While it is evident that rare-earth filling dramatically affects the thermal and electronic properties of these compounds, the role of Fe doping on the Co site is equally dramatic but as yet not well understood.

Various experiments have shown that Fe is paramagnetic in antimonide skutterudites. Danebrock, Evers, and Jeitschko[15] measured the magnetic properties of alkaline earth- and lanthanide-filled iron antimonide skutterudites and found paramagnetic effective Bohr magneton numbers of 2.6–2.8 μ_B/Fe atom for the alkaline earths and 3.0 μ_B/Fe atom for the lanthanides. These values are higher than that of the spin-only, low-spin d^5 configuration of Fe^{3+} and are attributed to spin-orbit coupling. Sales *et al.* studied the magnetic properties of $La_{0.9}Fe_3CoSb_{12}$,[16] and found a paramagnetic effective Bohr magneton number of 0.63 per transition metal atom (0.84 per Fe atom). Gajewski *et al.* investigated the magnetic properties of $Fe_{0.2}Co_{3.8}Sb_{12}$ and found a local moment.[17] The valence state and electron configuration of Fe in skutterudites, however, has yet to be clearly determined.

In most of these previous studies Fe doping and rare-earth filling were concomitant, thus preventing a direct study of the influence of Fe on the thermoelectric and magnetic properties. The outstanding issues we address here are: (1) the cause of the reduction in the thermal conductivity with Fe doping; and (2) the influence of Fe on the electronic structure of skutterudites. Such information is essential for optimizing these materials for thermoelectric applications. To shed some light on the role of Fe on the Co site in skutterudites, we fabricated a series of polycrystalline unfilled skutterudite samples of the form $Co_{1-x}Fe_xSb_3$ with $x=0$, 0.005, 0.01, 0.02, 0.05, and 0.1. Here we report our results of x-ray diffraction, chemical analysis, thermal conductivity, thermopower, electrical resistivity, Hall effect, and magnetization measurements. Although skutterudite compounds possess optimum thermoelectric properties at high temperatures, our measurements reported here have been carried out at room temperature and below because it is in this temperature range that the most information can be gleaned regarding the influence of Fe on the thermal and electronic properties. It is unlikely that this set of compounds will possess high figures of merit, but they present a simple means of isolating the direct influence of Fe on the thermoelectric properties, independent of any void-filling atom.

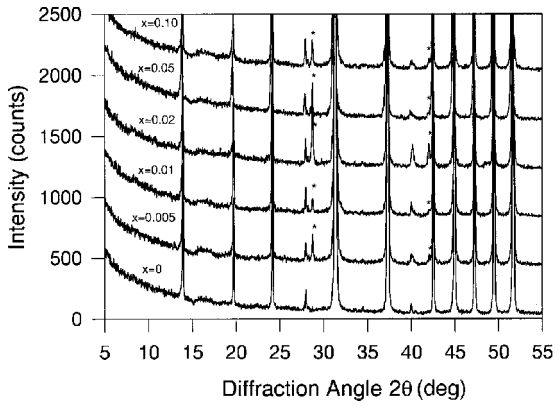

FIG. 1. X-ray powder diffraction spectra for $Co_{1-x}Fe_xSb_3$. A secondary phase, presumably Sb, is indicated by asterisks. Successive spectra are shifted by 500 counts for clarity, and the vertical scale is amplified to show the impurity phase peaks.

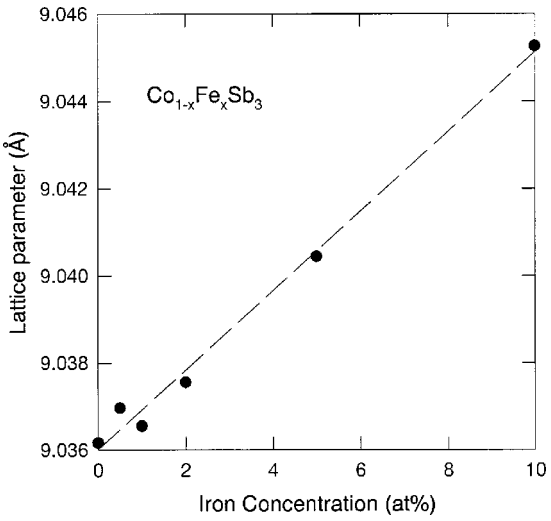

FIG. 2. Lattice parameters for $Co_{1-x}Fe_xSb_3$. The line is a guide for the eye.

II. EXPERIMENTAL TECHNIQUES

Polycrystalline samples of the form $Co_{1-x}Fe_xSb_3$ were made by induction melting of the high purity constituents at about 1400 °C. Samples were then annealed at 700 °C under argon for 20 h to achieve homogeneity and to crystallize the skutterudite phase. Sample stoichiometry was checked by wet etching chemical analysis as well as electron probe microanalysis (EPMA). A transmission electron microscopy (TEM) study was carried out on a Philips 430t TEM for the $Co_{0.9}Fe_{0.1}Sb_3$ sample to examine the subgrain precipitates. X-ray powder diffraction was performed on a Philips diffractometer using Cu K_α radiation to determine the crystalline phases and the skutterudite lattice parameters. Thermal conductivity κ, thermopower S, and electrical resistivity ρ measurements were made from 2 to 300 K in a cryostat equipped with a radiation shield. A longitudinal steady-state technique was used, and all samples had dimensions $3\times3\times10\,mm^3$. The method employs a strain gauge heater as a heat source and chromel-constantan thermocouples to determine the temperature gradient along the sample. Thin (25 μm diameter) Cu wires were used as voltage probes. The measured Seebeck coefficient S was corrected for the contribution from the Cu wires.[18,19] The absolute uncertainty in κ, S, and ρ is estimated to be less than 10%. Hall effect measurements were performed from 5 to 300 K in a cryostat equipped with a 5.5 T supeconducting magnet. Data were taken for both positive and negative magnetic fields to eliminate effects due to probe misalignment. Magnetization curves were measured from 10 to 300 K in applied field of up to 5 T using a Quantum Design magnetometer.

III. RESULTS AND DISCUSSION

A. Structural and chemical analysis

Figure 1 shows the results of standard θ-2θ x-ray diffraction scans. All samples show all the peaks characteristic of unfilled skutterudites plus some very small Sb peaks, which are indicated by asterisks in Fig. 1. The ratio between the highest Sb peak and the highest skutterudite peak is about a few percent, and we anticipate a smaller volume percentage of Sb phase in the samples because of the much greater number and intensity of peaks from the skutterudite phase compared to those of Sb. This Sb impurity has been reported before in binary skutterudites.[20] No other secondary phases were detected in x-ray diffraction measurements. The lattice parameters determined from the skutterudite diffraction peaks[21] are plotted in Fig. 2 and show a linear increase with increasing Fe concentration, following Vegard's law. This is consistent with the majority of Fe atoms going into the $CoSb_3$ lattice substitutionally for Co with a solubility of at least 10 at. %. All six samples were analyzed by EPMA. Backscatter electron imaging and optical micrography revealed that the overwhelming majority of each sample was single phase. A small, relatively rare, minor phase identified as Sb was detected in Fe-doped samples. No other secondary phases were detected by EPMA. The major phase of each of the samples was analyzed at eight random locations. Atomic compositions and the standard deviations are listed in Table I. Chemical composition analysis results are also listed in Table I. All samples are very close to stoichiometry. The sample with the greatest amount of Fe, i.e., $Co_{0.9}Fe_{0.1}Sb_3$, was analyzed by TEM. The bright field images, electron diffraction data, and x-ray spectroscopy data indicated that the sample is single phase in all areas examined. No subgrain precipitates were observed.

B. Magnetization

We performed magnetization measurements in order to help discern the charge state and the electron configuration of Fe in the skutterudite lattice. A direct measurement of this has not been possible because in all previous studies the magnetization measurements have been complicated by the presence of void filling atoms. The valence of Fe in skutterudites remains an unanswered question and is crucial for determining the electronic properties. To see why this is so, we

TABLE I. The nominal composition, the composition from chemical analysis, and the composition with its standard deviation derived by EPMA.

Nominal composition	Composition from chemical analysis	Composition from EPMA
$CoSb_3$	$CoSb_{2.995}$	$CoSb_{2.986\pm0.017}$
$Co_{0.995}Fe_{0.005}Sb_3$	$Co_{0.995}Fe_{0.005}Sb_{3.002}$	$Co_{0.995}Fe_{0.0050\pm0.0006}Sb_{2.980\pm0.022}$
$Co_{0.99}Fe_{0.01}Sb_3$	$Co_{0.990}Fe_{0.009}Sb_{3.030}$	$Co_{0.990}Fe_{0.0090\pm0.0012}Sb_{2.990\pm0.016}$
$Co_{0.98}Fe_{0.02}Sb_3$	$Co_{0.980}Fe_{0.019}Sb_{2.987}$	$Co_{0.980}Fe_{0.0199\pm0.0018}Sb_{2.981\pm0.018}$
$Co_{0.95}Fe_{0.05}Sb_3$	$Co_{0.950}Fe_{0.048}Sb_{2.996}$	$Co_{0.950}Fe_{0.0497\pm0.0041}Sb_{3.005\pm0.025}$
$Co_{0.9}Fe_{0.1}Sb_3$	$Co_{0.900}Fe_{0.095}Sb_{2.974}$	$Co_{0.900}Fe_{0.0981\pm0.0052}Sb_{3.004\pm0.026}$

undertake a brief discussion of the structure and bonding in binary skutterudite compounds.

In the skutterudite structure, each X (in this case, Sb) atom has four nearest neighbors, two metal atoms and two nonmetal atoms, situated at the corners of a distorted tetrahedron. Both the M-X bond distances and the X-X bond distances are short and nearly equal to the sum of the covalent radii, indicating strong covalent bonding. Given this structural information, most authors have described the bonding arrangement, with minor deviations, as follows: each X atom, which possesses five valence electrons, bonds with its two nearest X neighbors via σ bonds, thereby involving two of its valence electrons. The remaining valence electrons of the X atoms (three per atom) participate in the two M-X bonds. Since each metal atom is octahedrally coordinated by X atoms, there are a total of $(3/2)\cdot 6=9$ X electrons available for bonding in each MX_6 octahedron. In $CoSb_3$ the M atom possesses a s^2d^7 configuration and can provide an additional nine electrons, so that there are a total of 18 electrons available for this M-X arrangement. These are assumed to form d^2sp^3 hybrid bonds. The octahedral ligand field of the X atoms splits the degenerate *d* level into three lower energy nonbonding orbitals and two higher energy orbitals which hybridize with the metal atom *s* and *p* states to form the *dps* orbital complex which provides the M-X bonding. Of the 18 electrons available for bonding, six fill the nonbonding orbitals in a spin-paired arrangement, while the remaining 12 fill the hybridized *dps* complex. Thus it is expected that $CoSb_3$ will contain no unpaired spins or free electrons and therefore will be a diamagnetic semiconductor, and this is what is observed. Iron (s^2d^6 configuration) possesses one less electron compared to Co. The extent to which this affects the electronic properties depends on whether the Fe ion assumes the zero-spin $Fe^{2+}(d^6)$ or low-spin $Fe^{3+}(d^5)$ state.

For our $Co_{1-x}Fe_xSb_3$ samples, we observed the magnetization curves to contain a small ferromagnetic contribution that we presume is due to an iron-based impurity phase. We have analyzed our magnetization data by taking into account diamagnetic (lattice), paramagnetic (Curie-Weiss), and ferromagnetic (saturable) components. The total magnetic moment can therefore be written as

$$M_{\text{total}}=M_d+M_{\text{PM}}+M_{\text{FM}}, \tag{1}$$

where M_{total}, M_d, M_{PM}, and M_{FM} are the total, diamagnetic, paramagnetic, and ferromagnetic moments, respectively. To separate out the contribution of the ferromagnetic component, we extracted the differential magnetic susceptibility $\chi_{\text{total}}=\partial M_{\text{total}}/\partial H$ for each temperature at magnetic field $H=4$ T. At this high applied magnetic field M_{FM} saturates and $\partial M_{\text{FM}}/\partial H=0$. The ferromagnetic component M_{FM} is consistent with a very small fraction of the Fe in our samples being α-Fe. This secondary phase was not detected by x-ray diffraction mainly because the percentage of the α-Fe is small compared to the total amount of Fe in the samples and because the strongest x-ray diffraction peak overlaps with the strong skutterudite peak at $2\theta\approx 45°$. The percentage of Fe present as an α-Fe impurity can be estimated as $M_{\text{FM}}/(2.22\,\mu_B/\text{Fe})$, where M_{FM} is the measured ferromagnetic moment per Fe atom in each sample and the saturation magnetic moment of Fe atoms with metallic bonds is $2.22\,\mu_B/\text{Fe}$.[22] The percentage of α-Fe roughly decreases with increasing Fe doping in the samples. In the 0.5 at. % Fe-doped sample, the α-Fe percentage is about 10.5% (of the total 0.5 at. %). It drops to about 3.6% (of the total 10 at. %) for the sample with 10 at. % Fe doping. The corrected Fe composition x_{corr} representing the Fe content in the skutterudite phase is given by

$$x_{\text{corr}}=x\left(1-\frac{M_{\text{FM}}}{2.22\mu_B/\text{Fe}}\right), \tag{2}$$

and Table II shows our results for M_{FM} and x_{corr}.

Our magnetization results indicate that our pure $CoSb_3$ sample is, as expected, diamagnetic, consistent with a Co^{3+} zero-spin d^6 electron configuration. Figure 3 displays the present results for the susceptibility χ_{pure} of $CoSb_3$ as a function of temperature and includes, for comparison, results of a previous sample of $CoSb_3$.[10] There is some sample variation in both the temperature independent diamagnetic contribution and the amount of a small Curie-Weiss type paramagnetic contribution that becomes evident at low temperatures. The magnetization curves for the present sample of $CoSb_3$ are linear with field up to 5 T, and there is no evidence for an impurity ferromagnetic component. The overall temperature dependence of the susceptibilities of the two samples is very similar. The fact that they differ approximately by a constant indicates that the measured susceptibility is somewhat sample dependent and may depend on effective doping levels present in nominally ''undoped'' samples. The difference

TABLE II. Magnetic properties and fitting parameters of $Co_{1-x}Fe_xSb_3$. The corrected Fe composition x_{corr} is the nominal Fe composition x adjusted using Eq. (2) for an α-Fe type impurity phase as measured by M_{FM}. The fitting parameters to Eq. (3) for the total paramagnetic susceptibility χ_{total} are B, C, and θ_{CW}, and P is the effective Bohr magneton number per Fe atom derived from C using Eq. (4). The fitting parameters to Eq. (5) for the paramagnetic susceptibility per Fe atom χ are χ_0', C', and θ_{CW}, and P' is the effective Bohr magneton number derived from C' using Eq. (4).

x	0	0.005	0.01	0.02	0.05	0.1
$M_{FM}(\mu_B/\text{Fe})$	0	0.234	0.025	0.151	0.053	0.080
x_{corr}	0	0.0045	0.0099	0.019	0.049	0.096
$\chi_0(10^{-28}\,\text{cm}^3/\text{M atom})$	−1.79	−1.30	−1.13	−1.43	−0.25	0.40
$B(10^{-32}\,\text{cm}^3\,\text{K}^{-1}/\text{M atom})$	2.99	−9.92	4.66	−7.89	-24.6	−31.8
$C(10^{-28}\,\text{cm}^3\,\text{K/M atom})$	13.6	1.86	40.4	86.9	232	534
θ_{CW} (K)	29.8	−5.73	0.69	1.81	2.38	6.26
$P(\mu_B/\text{Fe})$	—	0.446	1.40	1.48	1.51	1.64
$\chi_0'(10^{-27}\,\text{cm}^3/\text{Fe})$	—	4.06	6.79	0.34	1.65	1.24
$C'(10^{-25}\,\text{cm}^3\,\text{K/Fe})$	—	0.888	3.14	4.80	5.25	6.03
θ_{CW} (K)	—	0	0	2.52	3.54	7.37
$P'(\mu_B/\text{Fe})$	—	0.654	1.23	1.52	1.59	1.70

in susceptibility between the two samples in Fig. 1, though seemingly large, is actually very small if we were to plot the data from Ref. 10 in Fig. 4.

Figure 4 shows the temperature dependence of χ_{total} for $Co_{1-x}Fe_xSb_3$ from 10 to 300 K. The lines represent the results from a fit to the data of the following formula:

$$\chi_{total}=\chi_0+B\cdot T+\frac{C}{T+\theta_{CW}}, \tag{3}$$

where χ_0 is the temperature-independent lattice susceptibility, $B\cdot T$ is a linear temperature-dependent lattice susceptibility, C is the Curie constant, and θ_{CW} is the Curie-Weiss temperature. The first two terms in Eq. (3) represent a model of the susceptibility which is unavoidably affected by the subtraction of the ferromagnetic component but nevertheless allows the isolation of the paramagnetic Curie-Weiss contribution to the susceptibility. We attempted to fit χ_{total} with $\theta_{CW}=0$, but the overall fit was not as good as that of nonzero θ_{CW}. There was no evidence of low temperature magnetic ordering above 10 K for any of our samples. The fitting parameters are listed in Table II together with the effective Bohr magneton number per Fe atom P calculated from

$$P=\frac{\sqrt{3k_BC/x_{corr}}}{\mu_B}, \tag{4}$$

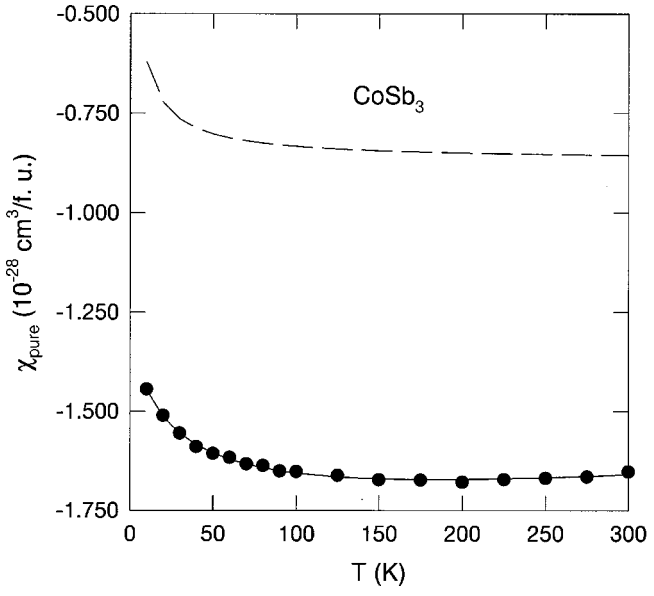

FIG. 3. The magnetic susceptibility of pure $CoSb_3$ vs temperature from 10 to 300 K. The dashed line represents the data for $CoSb_3$ from Ref. 10. The dots and the solid line are data for $CoSb_3$ and the fit using Eq. (3).

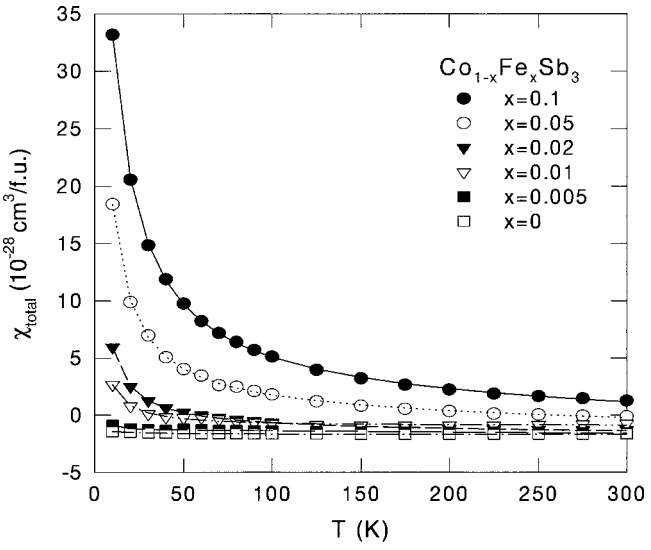

FIG. 4. The magnetic susceptibility χ_{total} vs temperature for $Co_{1-x}Fe_xSb_3$ from 10 to 300 K. The lines are least squares fits to the data using Eq. (3); the fitting parameters are listed in Table II.

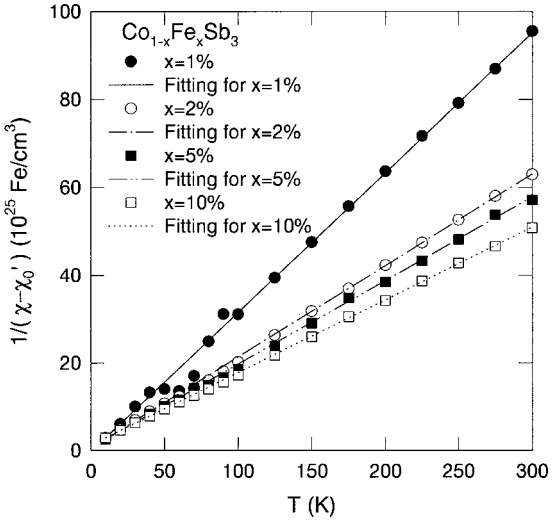

FIG. 5. The inverse magnetic susceptibility $1/(\chi-\chi_0')$ vs temperature for $Co_{1-x}Fe_xSb_3$. The lines are fits to the data according to Eq. (6). The susceptibility for $x=0.005$ is very close to the lattice susceptibility, and the subtraction according to Eq. (5) introduces a lot of scatter in the data. Consequently $1/(\chi-\chi_0')$ for $x=0.005$ is not plotted. The fit parameters for $x=0.005$ are included in Table II.

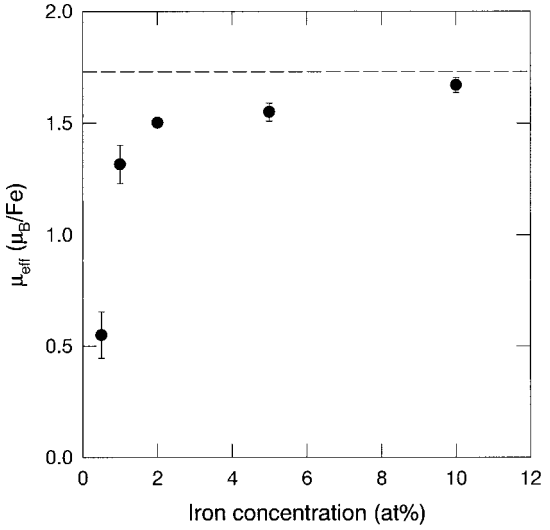

FIG. 6. The average effective Bohr magneton number $\mu_{\rm eff}=(P+P')/2$ vs Fe concentration. The dashed line is the magnetic moment $\mu_{\rm eff}=1.73\mu_B$/Fe expected for Fe in a low-spin d^5 electron configuration. The sizes of error bars are equal to $|P'-P|$.

where k_B is the Boltzmann constant and μ_B the Bohr magneton.

An alternative method of analyzing the magnetic susceptibility is to subtract the diamagnetic background susceptibility from $\chi_{\rm total}$ for each Fe-doped sample at each temperature in the following way:

$$\chi=\frac{\chi_{\rm total}-\chi_{\rm pure}}{x_{\rm corr}}, \tag{5}$$

where $\chi_{\rm pure}$ is our measured susceptibility of $CoSb_3$. Here, χ is the temperature-dependent magnetic susceptibility per Fe atom. The paramagnetic susceptibility χ for Fe-doped samples can be fit with the following simple expression:

$$\chi=\chi_0'+\frac{C'}{T+\theta_{CW}'}, \tag{6}$$

where χ_0' is the remaining temperature independent susceptibility per Fe atom, C' the Curie constant per Fe atom, and $\theta_{\rm CW}$ the Curie-Weiss temperature. Figure 5 shows that $1/(\chi-\chi_0')$ varies linearly with T for all $Co_{1-x}Fe_xSb_3$ samples. The fitting parameters are listed in Table II together with the effective Bohr magneton number P' calculated from the Curie constant C' and corrected for the ferromagnetic impurity phase as given in Eq. (4). The average effective Bohr magneton number $\mu_{\rm eff}=(P+P')/2$ is plotted as a function of Fe concentration in Fig. 6, where the sizes of the error bars are chosen to be $|P'-P|$. From Fig. 6, we observe an increasing $\mu_{\rm eff}$ with increasing Fe concentration. This indicates the development of a paramagnetic state of Fe in the $Co_{1-x}Fe_xSb_3$ samples upon Fe doping. Thus, after correcting for the ferromagnetic impurity phase, we observe a paramagnetic state in all Fe-doped samples with an effective moment $\mu_{\rm eff}$ that asymptotes to $\sim 1.7\mu_B$/Fe atom as a function of x. According to the formula $\mu_{\rm eff}=2[s(s+1)]^{1/2}\mu_B$ a magnetic moment of $1.73\mu_B$/Fe atom would be expected for a spin-only (orbital quenched) Fe^{3+} state, i.e., a low-spin d^5 system containing one unpaired electron in the lower energy nonbonding d orbitals. This implies that the number of valence electrons available for the M-X bonds for Fe in $Co_{1-x}Fe_xSb_3$ is the same as for Co.

C. Resistivity and carrier concentration

Figure 7 shows the temperature dependence of the resistivity of all the $Co_{1-x}Fe_xSb_3$ samples. Pure $CoSb_3$ has an activated behavior at low temperature and changes to a

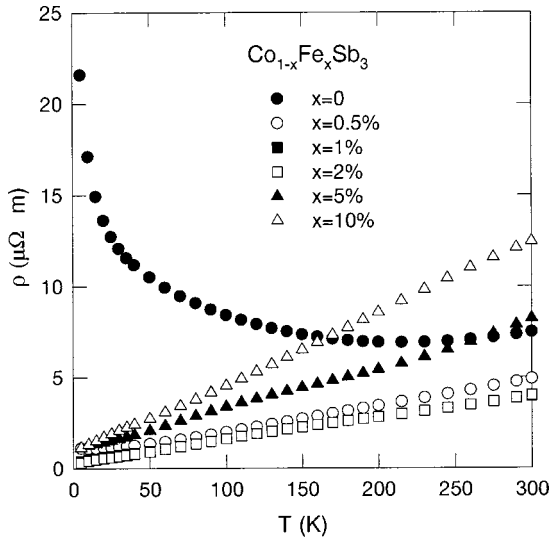

FIG. 7. Electrical resistivity of $Co_{1-x}Fe_xSb_3$ vs temperature from 2 to 300 K.

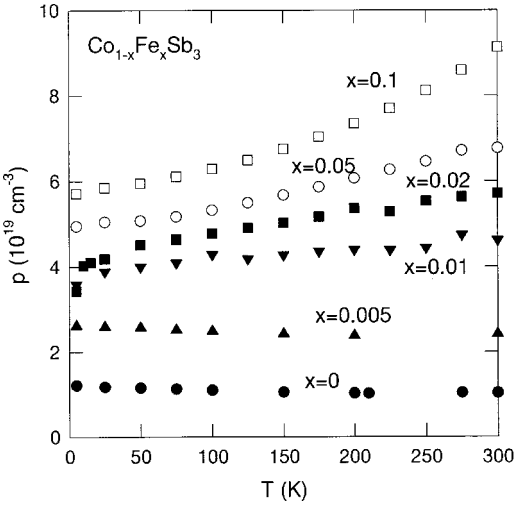

FIG. 8. Carrier concentration of $Co_{1-x}Fe_xSb_3$ vs temperature from 5 to 300 K.

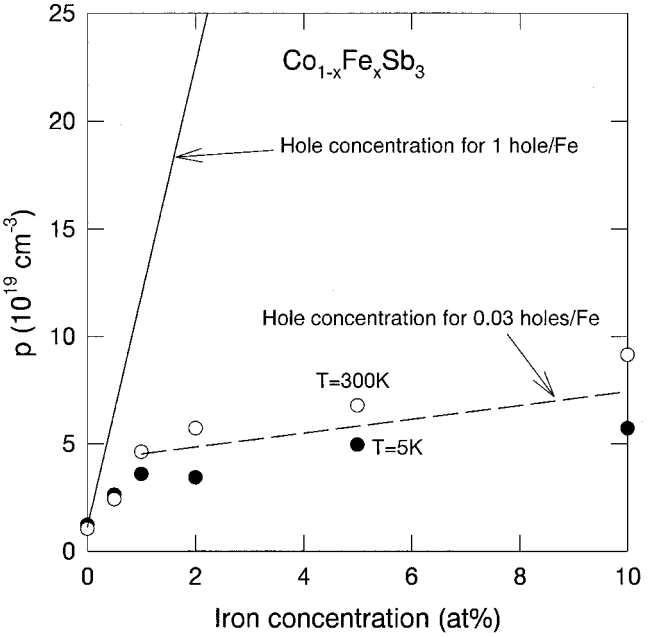

FIG. 9. Hole concentration vs iron concentration at 5 K (solid circles) and 300 K (open circles). The solid line is the calculated hole concentration for 1 hole/Fe expected for Fe^{2+}. The hole concentration rate of 0.03 holes/Fe (dash line) is the average slope of all the data for $x \geqslant 1$ at. %.

metallic-like character between 200 and 300 K. For all Fe-doped samples, the resistivity shows metallic behavior throughout the temperature range studied. The room temperature resistivity values vary from 4 to 13 $\mu\Omega$ m. The measured Hall resistance was positive and linear in magnetic field up to 5 T, indicating that a single *p*-type carrier dominates the electronic transport. The temperature dependence of the hole concentration is plotted in Fig. 8. The samples with higher Fe doping have higher hole concentrations throughout the whole temperature regime. For the pure $CoSb_3$ sample and the sample with $x=0.5$ at. %, the hole concentration decreases slightly with increasing temperature from 5 to 300 K. Samples with higher Fe concentration have increasing hole concentration with increasing temperature.

At room temperature, the hole concentration for pure $CoSb_3$ is about $1\times10^{19}\,cm^{-3}$ and that of the sample with $x=10$ at. % is about $9\times10^{19}\,cm^{-3}$. From our magnetic susceptibility results of the previous section, we should expect no change in hole concentration with doping by Fe^{3+} atoms. For comparison, if we assume iron is in an Fe^{2+} state, the hole concentration due to Fe doping would be equal to the number of Fe atoms per cm^3, which is equal to $x\cdot n_{Co}$, where n_{Co} is the number of Co atoms per cm^3 in $CoSb_3$. We estimate n_{Co} as $n_{Co}=d\cdot N_A/A$, where $d=7.582\,g/cm^3$ (Ref. 23) is the density of the sample, N_A is the Avogadro constant, and A is the atomic mass of the sample. For $x=10$ at. %, we have $x\cdot n_{Co}=1.07\times10^{21}\,cm^{-3}$, which is about an order of magnitude higher that the hole concentration we measured. Therefore, the carrier concentration we observe cannot be due to Fe^{2+} replacing Co^{3+}. Figure 9 shows the hole concentration at 5 and 300 K as a function of iron concentration for $Co_{1-x}Fe_xSb_3$. For samples with $x\leqslant1$ at. %, the hole concentrations at both temperatures increase approximately at a rate of 0.28 holes/Fe. As x increases ($x\geqslant1$ at. %), the rate at both temperatures reduces to approximately 0.03 holes/Fe. In principle, a 10% Fe^{2+} (of the total Fe) would give rise to the observed carrier concentration, but it could not account for the lattice thermal conductivity decrease that we will discuss in a later section. We conclude therefore that iron is essentially trivalent in $Co_{1-x}Fe_xSb_3$ for $x\geqslant1$ at. %. We shall see below from our thermal conductivity analysis that it is an increase in the concentration of vacancies on the Co site that gives rise to the increase of hole concentration with increasing iron concentration.

Figure 10 shows the temperature dependence of Hall mobility μ_H derived from the experimental hole concentration and resistivity. Above 100 K, we observe a $T^{-1.5}$ dependence. This is an indication that the dominant scatterers of the holes are phonons[24] as has been previously suggested by Morelli *et al.* for pure $CoSb_3$.[25] The lack of $T^{1.5}$ dependence for ionized impurity scattering at low temperature may be due to the screening effect as speculated in Ref. 25.

D. Thermopower

Figure 11 shows the temperature dependence of the Seebeck coefficient S for these $Co_{1-x}Fe_xSb_3$ samples. In addition to the diffusive S, which is linear in T, a phonon drag effect is observed at low temperature for $x=0$, 0.5, and 2 at. %. We identify these features as phonon drag because of their coincidence with the temperature of the peak in the thermal conductivity (which will be discussed in the next section). The room temperature Seebeck coefficients are plotted in Fig. 12 as a function of the hole concentration. Our data fit well with the $S\sim p^{-1/3}$ dependence predicted by Singh and Pickett.[26]

E. Thermal conductivity

The total thermal conductivity of a solid can be written as

$$\kappa_T=\kappa_L+\kappa_e, \tag{7}$$

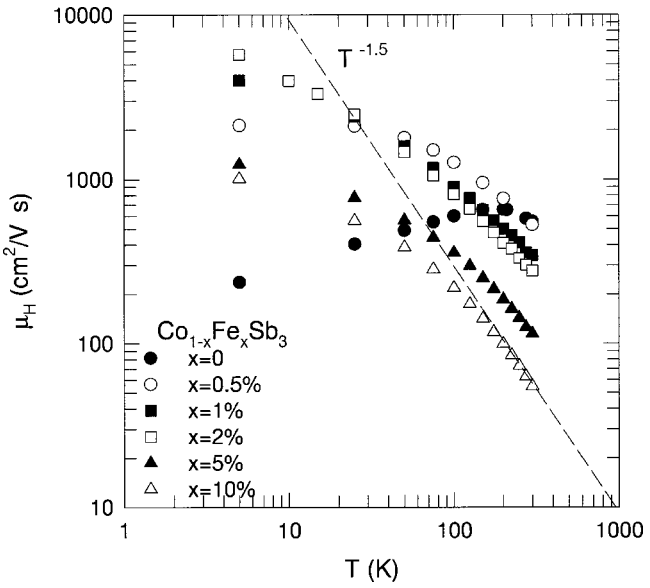

FIG. 10. Temperature dependence of Hall mobility for the $Co_{1-x}Fe_xSb_3$. The dashed line shows the $T^{-1.5}$ temperature dependence that is observed for Fe-containing samples at 100 K and above.

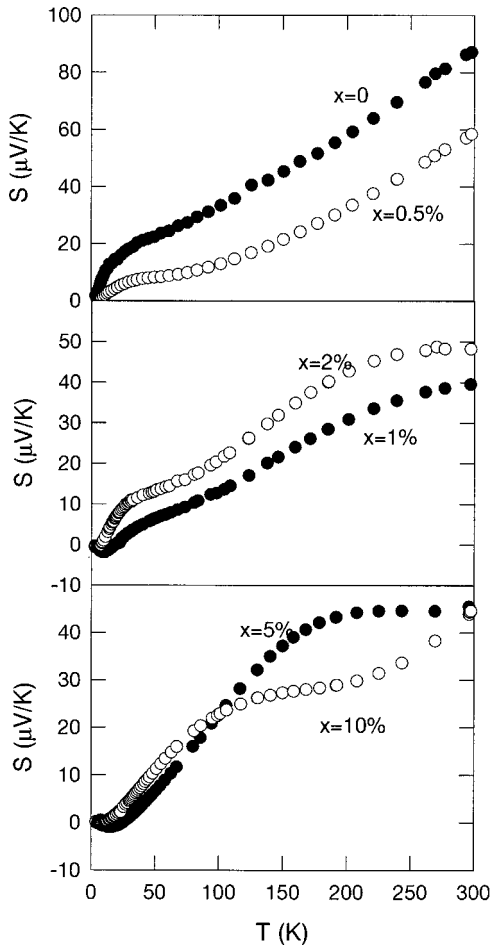

FIG. 11. Temperature dependence of the thermopower S for $Co_{1-x}Fe_xSb_3$.

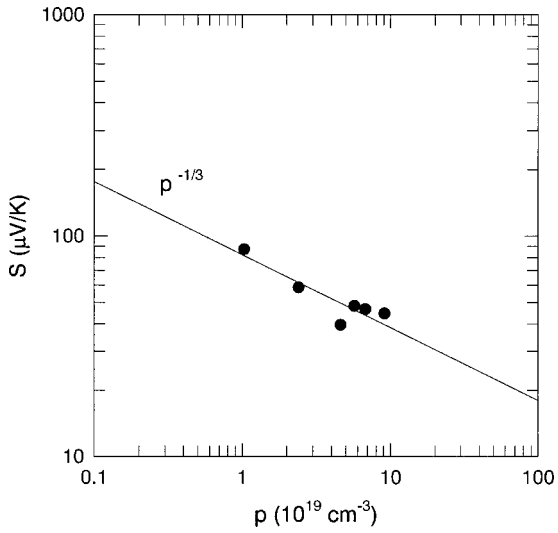

FIG. 12. Room temperature thermopower vs hole concentration for $Co_{1-x}Fe_xSb_3$. The solid line is the $S \sim p^{-1/3}$ dependence.

where κ_T, κ_L, and κ_e are the total, lattice, and carrier thermal conductivities, respectively. According to the Wiedemann-Franz law, the carrier thermal conductivity κ_e can be estimated from

$$\kappa_e = L_0 T/\rho, \tag{8}$$

where ρ is the electrical resistivity, T is temperature, and the Lorenz number L_0 has a numerical value of $2.45 \times 10^{-8}\,V^2/K^2$. Hence, the lattice thermal conductivity can be found by subtracting the carrier component from the measured total thermal conductivity. Figure 13 shows the lattice thermal conductivity plotted as a function of temperature for all six samples, and the temperature dependence is what one would expect for a dielectric solid. Phonon scattering is dominated by boundary scattering at low temperatures, by defect scattering at intermediate temperatures, and by Umklapp processes at high temperatures. The peak value of the

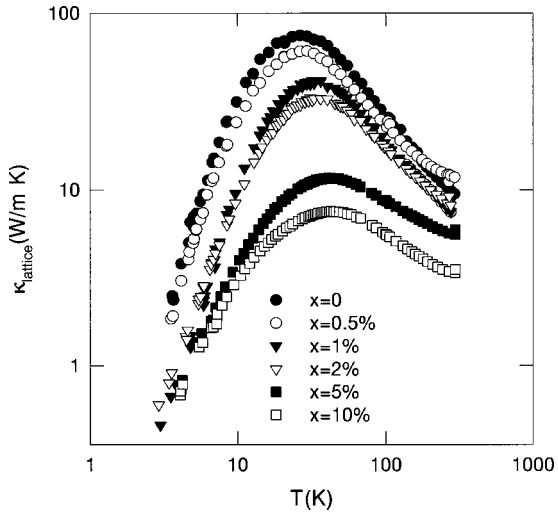

FIG. 13. Lattice thermal conductivity of $Co_{1-x}Fe_xSb_3$ vs temperature.

lattice thermal conductivity decreases dramatically as the Fe doping level increases, decreasing from 74.8 W/m K for undoped $CoSb_3$ to 7.53 W/m K for $Co_{0.9}Fe_{0.1}Sb_3$. Thus 10 at. % Fe on the Co site leads to an order of magnitude reduction of the lattice thermal conductivity. This is a rather surprising result because the mass and the size differences between Co and Fe are only 5% and 6%, respectively. The additional strain and mass fluctuations introduced by alloying Fe on the Co site will reduce the lattice thermal conductivity, but they would not cause an order of magnitude reduction. In order to clarify the role of Fe in strongly enhancing phonon scattering, we modeled the temperature dependence of the lattice thermal conductivity for all the samples. According to the calculation, lattice defect scattering has a strong influence on the lattice thermal conductivity.

Thermal conduction is usually treated using the Debye approximation. In this model, the lattice thermal conductivity can be written as[27,28]

$$\kappa_L = \frac{k_B}{2\pi^2 \nu}\left(\frac{k_B}{\hbar}\right)^3 T^3 \int_0^{\theta_D/T} \frac{\tau_c x^4 e^x}{(e^x-1)^2}\,dx, \tag{9}$$

where $x=\hbar\omega/k_BT$ is dimensionless, ω is the phonon frequency, k_B is the Boltzmann constant, $\hbar$ is the Planck constant, θ_D is the Debye temperature, ν is the velocity of sound, and τ_c is the relaxation time. The overall relaxation rate τ_c^{-1} can be determined by combining various scattering processes

$$\tau_c^{-1} = \tau_B^{-1} + \tau_D^{-1} + \tau_U^{-1}, \tag{10}$$

where τ_B, τ_D, and τ_U are the relaxation times for boundary scattering, defect scattering, and Umklapp processes, respectively. The boundary scattering rate is

$$\tau_B^{-1} = \nu/L, \tag{11}$$

where L is the sample grain size. For the defect scattering we use the Rayleigh point defect rate

$$\tau_D^{-1} = A\omega^4, \tag{12}$$

where A is independent of temperature. Umklapp processes are characterized by a relaxation rate proposed by Glassbrenner and Slack (GS) for Ge and Si[29]

$$\tau_U^{-1} = B\omega^2 T \exp(-\theta_D/3T), \tag{13}$$

which we designate as the GS Umklapp model. This model has been used successfully for diamond[30] and other materials.[25] Figure 14 shows the measured and the calculated lattice thermal conductivity for the $x=0$ sample. The dotted line is computed using Eqs. (9)–(13) with $\theta_D=287$ K and $\nu=2700$ m/s,[25] and the fitting parameters are listed in Table III. As Fig. 14 indicates, the dotted line fits the measured values very well for $T<100$ K, but it underestimates lattice thermal conductivity for $T>100$ K. This is true for all the samples we studied (see Fig. 15). We attempted to include normal scattering[27,28] in the calculations, but it did not improve the overall fit. We also tried to include electron-phonon interaction[31] in our calculation, and we found that electron-phonon interaction in these *p*-type skutterudites is not a significant factor.[32] The discrepancy between the data and fit at $T>100$ K may be due to a variety of reasons: radiation losses, temperature dependence of the Lorenz number,[33] and deviation of the thermal conductivity from the $1/T$ temperature dependence at high temperature.[34] This discrepancy, however, will not affect the following analysis.

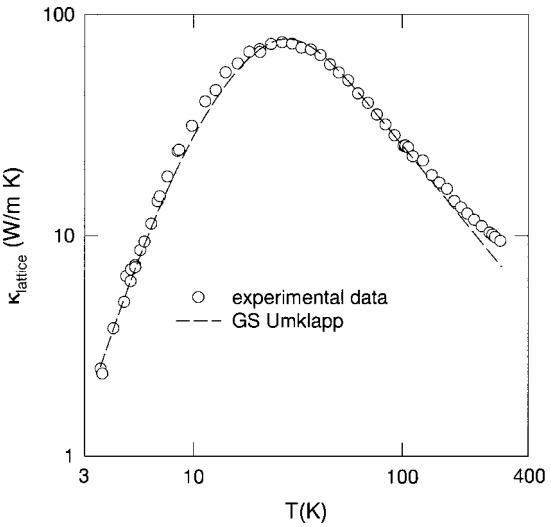

FIG. 14. Experimental and calculated lattice thermal conductivity for $CoSb_3$ vs temperature. The open circles are the experimental data. The dotted line represents a calculation based on the GS Umklapp model.

Table III lists the fitting parameters of our calculation for all six samples. The grain size for the samples varies from about 2 to 10 μm with no obvious trend among the samples. The Umklapp prefactor B is chosen to be the same for all the samples. From a lattice point of view, Fe and Co are very similar. Umklapp scattering should not vary significantly by replacing Co with Fe. In addition, Debye temperature is a crucial parameter that determines the Umklapp scattering rate. Recent work by Long *et al.*[35] shows that Debye temperatures for a series of samples of the form $Ce_xFe_{4-y}Co_ySb_{12}$ indeed do not vary significantly in a wide phase space of x and y. We feel it is a good approximation to assume that Umklapp scattering rate remains the same for our $Co_{1-x}Fe_xSb_3$ samples. The prefactor A for point defect scattering increases with increasing Fe doping level except that A for the 1 at. % doped sample is slightly lower than that of the 0.5 at. % doped sample. In Fig. 16, A is plotted as a function of Fe doping level. According to Klemens,[36] A is

TABLE III. Lattice thermal conductivity fitting parameters for $Co_{1-x}Fe_xSb_3$ as defined by Eqs. (11), (12), and (13).

x	L (μm)	A (10^{-43} s^3)	B (10^{-18} s/K)
0	10.54	2.79	5.38
0.005	10.86	4.52	5.38
0.01	3.18	4.36	5.38
0.02	3.11	6.73	5.38
0.05	3.23	37.10	5.38
0.1	2.36	77.27	5.38

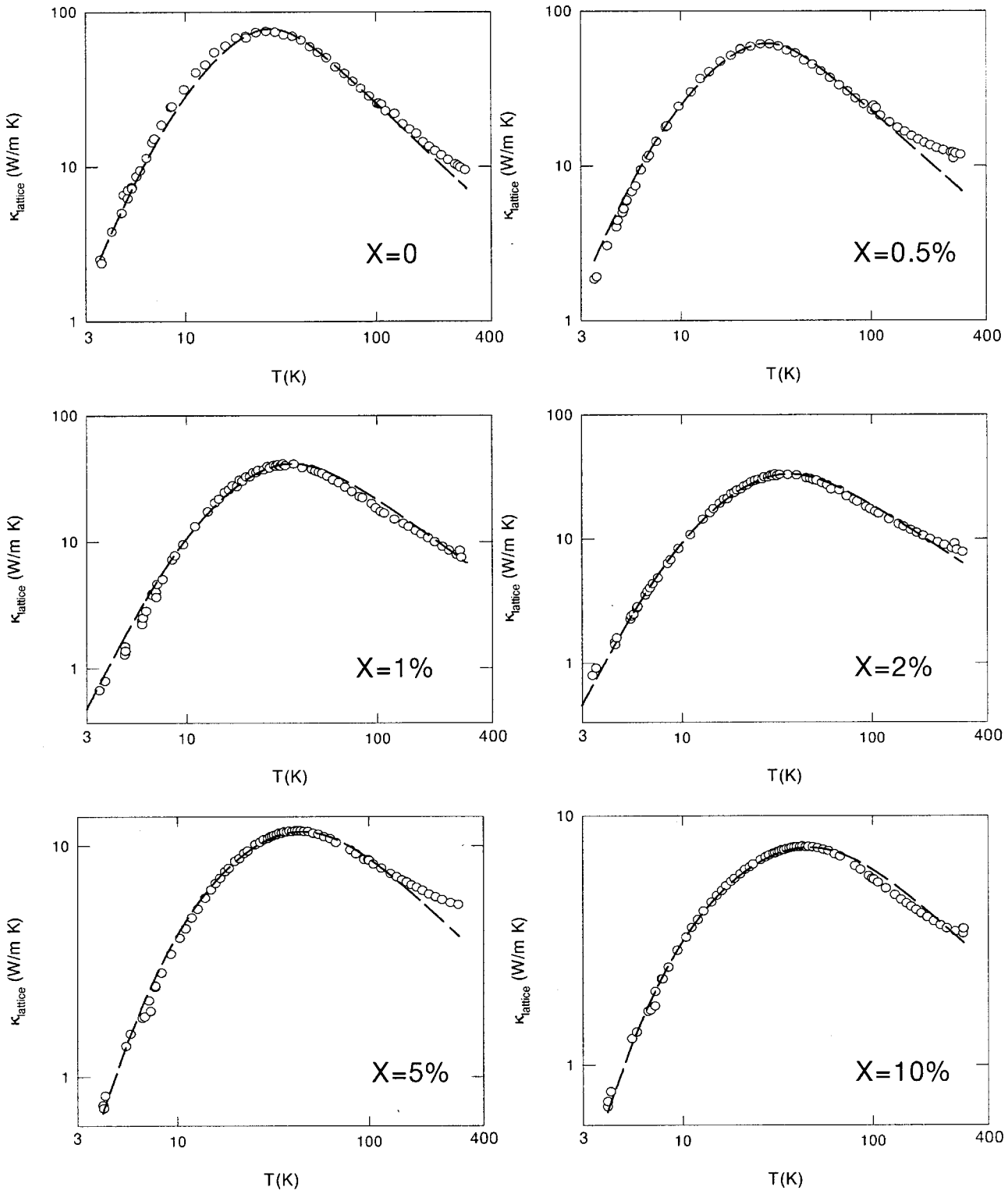

FIG. 15. Lattice thermal conductivity of $Co_{1-x}Fe_xSb_3$ vs temperature. The open circles are experimental data. Dotted lines are calculations using the GS Umklapp model.

proportional to $c(1-c)$, where c is the relative concentration of point defects. Hence, A increases monotonically with increasing c for small c. This implies that the point defect concentration in $Co_{1-x}Fe_xSb_3$ increases with increasing Fe doping level. Early work by Dudkin and Abrikosov[37] suggested that lattice defects, most likely vacancies, exist in p-type $CoSb_3$ because of excess Sb. We believe that the decrease of thermal conductivity with increasing Fe concentration is a direct consequence of the increase in concentration of these point defects indicated by the increasing A value with x determined from the fits to the data. If we take our analysis one step further by assuming the measured hole con-

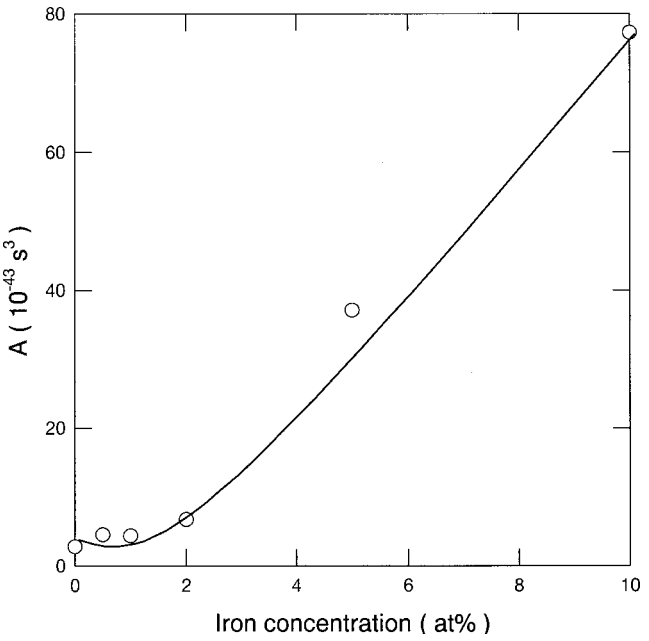

FIG. 16. The point defect scattering rate coefficient A vs Fe concentration. The deviation from a linear dependence at low Fe concentration indicates a background point defect concentration in pure $CoSb_3$.

centration is entirely due to the vacancies on the Co site, the vacancy density will be $p/3$. Therefore $c=p/(3\cdot n_{\mathrm{Co}})$. The prefactor A for point defect scattering can be written as

$$A=\Omega_0\Gamma/(4\pi v^3), \tag{14}$$

where Ω_0 is the unit cell volume and Γ is the scattering parameter. According to Refs. 14 and 38,

$$\Gamma(\mathrm{Co}_{1-x}\mathrm{Fe}_x\mathrm{Sb}_3)\approx(58.93/106.05)^2\Gamma(\mathrm{Co})/4, \tag{15}$$

where $\Gamma(\mathrm{Co})=c(1-c)[(\Delta M/M)_{\mathrm{eff}}]^2$. $(\Delta M/M)_{\mathrm{eff}}=1$ for zero-mass substitutional impurity and $(\Delta M/M)_{\mathrm{eff}}=3$ for vacancies with severed atomic bonds, as argued by Ratsifaritana and Klemens.[39,40] Therefore, we have

$$A\approx\Omega_0(58.93/106.05)^2c(1-c)[(\Delta M/M)_{\mathrm{eff}}]^2/[4(4\pi v^3)]. \tag{16}$$

If we use the A values from our thermal conductivity fitting, we can calculate $(\Delta M/M)_{\mathrm{eff}}$ for all of our six samples. These results are plotted in Fig. 17, which shows that $(\Delta M/M)_{\mathrm{eff}}$ increases with increasing Fe doping. This indicates that increasing number of vacancies with severed atomic bonds are introduced into the samples with increasing Fe doping. These vacancies with severed atomic bonds strongly decouple themselves from the host lattice. This in turn significantly enhances phonon scattering and consequently decreases the thermal conductivity. Harris, Enck, and Youngman observed similar effects for AlN.[41] The lower and upper limits for $(\Delta M/M)_{\mathrm{eff}}$ in Eq. (16) are 1 (zero-mass substitutional impurity) and 3 (vacancies with severed atomic bonds), respectively, and our calculated $(\Delta M/M)_{\mathrm{eff}}$ values are mostly within these limits. This tells us that our assumption that the hole concentration in our samples is due to vacancies on the

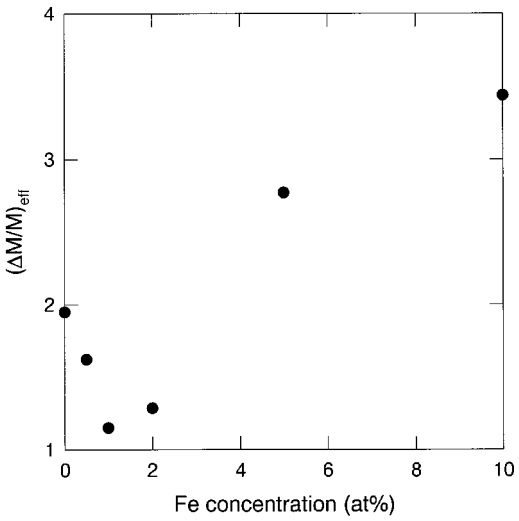

FIG. 17. $(\Delta M/M)_{\mathrm{eff}}$ vs Fe concentration for $\mathrm{Co}_{1-x}\mathrm{Fe}_x\mathrm{Sb}_3$.

Co site is reasonable. From our analysis of the magnetic properties, hole concentration, thermal conductivity, and calculation of $(\Delta M/M)_{\mathrm{eff}}$, we conclude that the hole concentration in $\mathrm{Co}_{1-x}\mathrm{Fe}_x\mathrm{Sb}_3$ we observe is due entirely to the lattice vacancies on the Co site. Increased Fe doping increases the number of vacancies on the Co site in the Skutterudites, and it is these vacancies that give rise to the reduction of the heat conduction. The increasing number of vacancies with severed atomic bonds due to the presence of Fe is reasonable in light of the eventual instability of the Skutterudite structure at higher Fe concentration and the lack of existence of a $FeSb_3$ phase. Recently reported electron tunneling experiments on $\mathrm{Co}_{1-x}\mathrm{Fe}_x\mathrm{Sb}_3$ (Ref. 42) suggest that the observed strong zero-bias conductance anomaly arises from a structural disorder such as vacancies on the Co sites, further corroborating our point of view.

IV. SUMMARY

We have studied the transport properties of $\mathrm{Co}_{1-x}\mathrm{Fe}_x\mathrm{Sb}_3$ samples from 2 to 300 K. All samples are p type with hole concentrations increasing with Fe doping level at a relatively small rate of $\sim$0.03 holes/Fe for $x\geqslant 1$ at. %. At room temperature, ZT (dimensionless figure of merit) values are between 0.01 and 0.03. Magnetization studies indicate that the substitutional Fe atoms assume a low spin d^5 configuration in the lattice with a paramagnetic moment approaching $1.73\mu_B$/Fe. We conclude from these results that iron is in a trivalent state in antimonide skutterudites. The thermal conductivity of $CoSb_3$ is dramatically suppressed with Fe doping due to an increase in lattice defects, most likely vacancies on the Co site of the skutterudite structure. These same lattice defects also alter the electronic properties of these Fe-doped skutterudites, providing three holes per defect. This suppression of thermal conductivity by Fe doping partially accounts for the high figure of merit in filled skutterudite compounds. Further optimization of these and other materials may lead to their application in advanced thermoelectric energy conversion devices and systems.

ACKNOWLEDGMENTS

J.Y. would like to thank Dr. P. G. Klemens for reading the original manuscript and many fruitful suggestions, Dr. G. A. Slack for many valuable discussions, Dr. J. F. Herbst for encouragement and support throughout this work, Dr. M. P. Balogh and Dr. R. A. Waldo for assisting the TEM and EPMA measurements, and General Motors for providing financial support. This work was also supported in part by DARPA under Contract No. N00014-98-3-0011.

[1] G. S. Nolas, D. T. Morelli, and T. Tritt, Annu. Rev. Mater. Sci. **29**, 89 (1999); C. Uher, in *Semiconductors and Semimetals*, Vol. 69, *Recent Trends in Thermoelectric Materials Research*, edited by T. M. Tritt (Academic, San Diego, 2000), pp. 139–253.
[2] I. Oftedal, Z. Kristallogr. **A66**, 517 (1928).
[3] W. Jeitschko and P. C. Donohue, Acta Crystallogr., Sect. B: Struct. Crystallogr. Cryst. Chem. **B31**, 575 (1975).
[4] J. Ackermann and A. Wold, J. Phys. Chem. Solids **38**, 1013 (1977).
[5] G. A. Slack and V. Tsoukala, J. Appl. Phys. **76**, 1665 (1994).
[6] D. T. Morelli and G. P. Meisner, J. Appl. Phys. **77**, 3777 (1995).
[7] B. C. Sales, D. Mandrus, and R. K. Williams, Science **272**, 1325 (1996).
[8] B. C. Sales, B. C. Chakoumakos, and D. Mandrus, Phys. Rev. B **61**, 2475 (2000).
[9] G. S. Nolas, M. Kaeser, R. T. Littleton, T. M. Tritt, H. Sellinschegg, D. C. Johnson, and E. Nelson, Mater. Res. Soc. Symp. Proc. **626**, Z10.1 (2000).
[10] D. T. Morelli, G. P. Meisner, B. Chen, S. Hu, and C. Uher, Phys. Rev. B **56**, 7376 (1997).
[11] G. S. Nolas, J. L. Cohn, and G. A. Slack, Phys. Rev. B **58**, 164 (1998).
[12] K. L. Stokes, A. C. Ehrlich, and G. S. Nolas, Mater. Res. Soc. Symp. Proc. **545**, 339 (1999).
[13] H. Anno, K. Matsubara, Y. Notohara, T. Sakakibara, and H. Tashiro, J. Appl. Phys. **86**, 3780 (1999).
[14] G. P. Meisner, D. T. Morelli, S. Hu, J. Yang, and C. Uher, Phys. Rev. Lett. **80**, 3551 (1998).
[15] M. E. Danebrock, C. B. H. Evers, and W. Jeitschko, J. Phys. Chem. Solids **57**, 381 (1996).
[16] B. C. Sales, D. Mandrus, B. C. Chakoumakos, V. Keppens, and J. R. Thompson, Phys. Rev. B **56**, 15 081 (1997).
[17] D. A. Gajewski, N. R. Dilley, E. D. Bauer, E. J. Freeman, R. Chau, M. B. Maple, D. Mandrus, B. C. Sales, and A. H. Lacerda, J. Phys.: Condens. Matter **10**, 6973 (1998).
[18] R. B. Roberts, Philos. Mag. **36**, 91 (1977).
[19] C. Uher, J. Appl. Phys. **62**, 4636 (1987).
[20] S. Katsuyama, Y. Shichijo, M. Ito, K. Majima, and H. Nagai, J. Appl. Phys. **84**, 6708 (1998).
[21] N. A. Razik, Appl. Phys. A: Solids Surf. **37**, 187 (1985).
[22] L. Pauling, *The Nature of Chemical Bond*, 3rd ed. (Cornell University Press, Ithaca, 1960), p. 397.
[23] T. Caillat, A. Borshchevsky, and J. P. Fleurial, J. Appl. Phys. **80**, 4442 (1996).
[24] K. Seeger, *Semiconductor Physics*, 4th ed. (Springer, New York, 1989).
[25] D. T. Morelli, T. Caillat, J.-P. Fleurial, A. Borshchevsky, J. W. Vandersande, B. Chen, and C. Uher, Phys. Rev. B **51**, 9622 (1995).
[26] D. J. Singh and W. E. Pickett, Phys. Rev. B **50**, 11 235 (1994).
[27] J. Callaway, Phys. Rev. **113**, 1046 (1959).
[28] J. Callaway, Phys. Rev. **120**, 1149 (1960).
[29] G. A. Glassbrenner and G. A. Slack, Phys. Rev. **134**, A1058 (1964).
[30] D. G. Onn *et al.*, Phys. Rev. Lett. **68**, 2806 (1992).
[31] J. M. Ziman, *Electrons and Phonons* (Oxford University Press, London, 1960).
[32] J. Yang (unpublished).
[33] P. G. Klemens, in *Thermal Conductivity*, edited by R. P. Tye (Academic, New York, 1969), Vol. 1.
[34] M. C. Roufosse and P. G. Klemens, J. Geophys. Res. **79**, 703 (1974).
[35] G. J. Long, D. Hautot, F. Grandjean, D. T. Morelli, and G. P. Meisner, Phys. Rev. B **60**, 7410 (1999).
[36] P. G. Klemens, Proc. Phys. Soc. London **A68**, 1113 (1959).
[37] L. D. Dudkin and N. Kh. Abrikosov, Sov. Phys. Solid State **1**, 126 (1959).
[38] G. A. Slack, Phys. Rev. **126**, 427 (1962).
[39] C. A. Ratsifaritana and P. G. Klemens, Int. J. Thermophys. **8**, 737 (1987).
[40] P. G. Klemens, Nucl. Instrum. Methods Phys. Res. B **1**, 204 (1984).
[41] J. H. Harris, R. C. Enck, and R. A. Youngman, Phys. Rev. B **47**, 5428 (1993).
[42] J. Nagao, M. Ferhat, H. Anno, K. Matsubara, E. Hatta, and K. Mukasa, Appl. Phys. Lett. **76**, 3436 (2000).